Dispersion and attenuation of compressional waves in tight oil reservoirs: Experiments and simulations

Article *in* Applied Geophysics · March 2019
DOI: 10.1007/s11770-019-0748-3

5 authors, including:

Rupeng Ma
Hohai University

Jing Ba
Hohai University

José M Carcione
OGS Istituto Nazionale di Oceanografia e di Geofisica Sperimentale

APPLIED GEOPHYSICS, Vol.16, No.1 (March 2019), P. 33−45, 19 Figures.
DOI:10.1007/s11770-019-0748-3

Dispersion and attenuation of compressional waves in tight oil reservoirs: Experiments and simulations*

Ma Ru-Peng[1], Ba Jing♦[1], Carcione José Maria[1,2], Zhou Xin[1], and Li Fan[1]

Abstract: We performed ultrasonic experiments in specimens from a tight oil reservoir. The P-wave attenuation of fluid-saturated specimens was estimated by the spectral ratio method. The results suggest that at ultrasonic frequencies, most specimens have stronger attenuation under gas-saturated conditions than at water- or oil-saturated conditions. The P-wave attenuation positively correlates with permeability. Scanning electron microscopy observations and the triple-porosity structure model were used to simulate the wave propagation. The P-wave velocity dispersion and attenuation are discussed on the basis of the Biot, Biot–Rayleigh double-porosity medium, and the triple-porosity structure models. The results suggest that the Biot and Biot–Rayleigh models cannot explain the attenuation, whereas the triple-porosity structure model is in agreement with the experimental data. Furthermore, we infer that microcracks are common in a porosity of 5%–10%, and the size of microcracks increases in samples with higher porosity. However, the volume ratios of microcracks and clay inclusions remain constant regardless of porosity variations. The size of microcracks is significantly larger than the clay inclusions, and the bulk modulus of microcracks is lower than the bulk modulus of clays.
Keywords: porosity, Biot, Rayleigh, wave, dispersion, attenuation

Introduction

Tight oil reservoirs are important unconventional oil and gas resources characterized by low porosity, low permeability, complex pore structure, and strong heterogeneity. Previous studies have shown that the existence of fabric heterogeneities and pore fluids in conventional carbonate rocks and sandstones can lead to velocity dispersion and energy attenuation of elastic waves in porous media (Pride et al., 2004; Spencer and Shine, 2016). Tight oil reservoirs mainly comprise

Manuscript received by the Editor November 7, 2018; revised manuscript received February 12, 2019.
*This work was supported by the Specially Appointed Professor Program of Jiangsu Province, China, the National Natural Science Foundation of China (No. 41704109), the Fundamental Research Funds for the Central Universities, China. (No. 2016B13114).
1 School of Earth Sciences and Engineering, Hohai University, Nanjing, 211100, China.
2 Istituto Nazionale di Oceanografia e di Geofisica Sperimentale (OGS), Borgo Grotta Gigante 42c, Sgonico, Trieste 34010, Italy
♦ Corresponding author: Ba Jing (jba@hhu.edu.cn)

sandstones, siltstones, and carbonate rocks with silt or clay components. Compared with conventional reservoir rocks, the diameters of pore throats in tight oil reservoirs are smaller, the porosity and permeability are lower, and the clay content is higher. To date, there are only a few studies on the elastic wave characteristics of such rocks. Thus, the influence of pore structure and fluid properties on seismic wave attenuation and dispersion remains poorly understood. The relation between seismic waves and reservoir parameters and that between elastic parameters and attenuation could provide the basis for better resources prediction and fluid detection in tight oil reservoirs.

Fluids in porous media are generally considered responsible for P-wave velocity dispersion and energy attenuation (Johnston et al., 1979; Winkler, 1985; Sams et al., 1997). Owing to fabric heterogeneities and heterogeneous distribution of fluids in rocks, pressure gradients are generated in pore fluids when elastic waves pass through the rocks, resulting in wave-induced local fluid flow. Berryman and Milton (1991) generalized the Gassmann equation for describing the uniform pore structure in composite porous media with double-porosity structure. Pride and Berryman (2003a, 2003b) considered the local fluid flow induced by rock heterogeneities in the dynamic equations and developed a wave propagation model for double-porosity media. Sayar et al. (2017) derived an effective medium model for describing four dissipative mechanisms based on self-consistent theory. Marín-Moreno et al. (2017) presented a theoretical model of complex porous media with hydrates and analyzed the P-wave attenuation caused by local fluid flow between hydrates and pores and between pores with different aspect ratios. Ba et al. (2016) used the double-porosity structure model to describe the wave response in tight oil reservoirs with submicroscopic pore structure and the velocity dispersion observed in ultrasonic experiments. The abovementioned models are all based on certain assumptions. To investigate the wave responses of different types of reservoirs, it is necessary to establish appropriate rock physics models based on the corresponding reservoir characteristics.

Experiments have been conducted on different types of rocks under different experimental conditions to study the relation between elastic wave attenuation and rock physics parameters, such as porosity, permeability, and saturation (Adam et al., 2009; Chapman et al., 2016). Winkler and Nur (1979) considered that attenuation is more sensitive to fluid saturation than wave velocity in the Massillon sandstone. Toksöz et al. (1979) measured P- and S-wave attenuation in dry, fluid-saturated, and frozen sandstones and limestones by ultrasonic experiments. Johnston and Toksöz (1980) conducted an experimental study of 12 limestones, sandstones, and oil shales. Generally, it is believed that the attenuation in water-saturated rocks is stronger than that in dry rocks in ultrasonic frequencies. Experimental studies with wet granite and mudstone at sonic frequencies have also shown that the attenuation in the water-saturated state is stronger than in the dry state (Oh et al., 2011). Agersborg et al. (2008) studied the variation of P-wave attenuation in carbonate rocks saturated with different fluids at ultrasonic frequencies. The results suggest that the attenuation in gas-saturated rocks is less than that in water-saturated and oil-saturated rocks. The attenuation of elastic waves in conventional sandstones and carbonate rocks has been studied (Best and Sams, 1997; He et al., 2010; Kuteynikova et al., 2014; Borgomano et al., 2017). However, almost no experimental data on tight oil reservoirs with smaller grain size, lower permeability, and greater heterogeneity are available.

In this study, we selected rock samples from the Qingshankou Formation in Daqing. Ultrasonic experiments were performed to assess the P-wave attenuation and the effects of basic physical parameters on velocity and attenuation The triple-porosity structure model was used to simulate the effect of fabric heterogeneity and fluid properties on velocity dispersion and energy attenuation, and the experimental data were modeled to determine the correlations between P-wave velocity, attenuation, and heterogeneity.

Experiments

Tight oil reservoirs

The Qingshankou Formation, Songliao Basin, Gulong is mainly composed of coastal, shallow, and deep lacustrine sediments. The formation is divided into three subsections, Qingshankou 1, 2, and 3. High-quality source rocks in section Qingshankou 2 have wide and continuous distribution (Yang et al., 2017; Huang et al., 2017). The source rocks are siltstones and mudstones. The thickness of the source rocks is 70–110 m, the porosity is 4–12%, and the permeability is typically 0.01–0.5 mD, which makes them poor reservoirs. Residual intergranular pores are dominant; furthermore, microfractures and dissolved pores are present. Pore diameter is generally between 5 and 100 μm. Drilling and logging data suggest that lithology and physical properties greatly affect the distribution of oil; siltstone is generally oil-bearing in this area, whereas the oil-bearing capability of muddy siltstones and silty mudstones is lower, and the better the reservoir physical properties, the better the oil-bearing properties (Shi et al., 2015).

Samples were taken from the Qingshankou 2 section from a depth of 2200 m at 80 °C and the pore pressure between 22 and 30 MPa. Twelve rock samples of siltstones, muddy siltstones, and silty mudstones were used in this study. The rock physics parameters are listed in Table 1. On the basis of scanning electron microscopy (SEM) data, the samples are characterized by grain-supported structure. Detrital grains account for 80–90% of the total volume based on X-ray diffraction data; quartz content is 24–44%; plagioclase and potassium feldspar make up 34–60%; clay minerals, mainly illite, make up 2–12.5%. Figure 1 shows SEM photographs of sample K at different magnifications. Clearly, the pore connectivity is poor.

Table 1. Physical parameters of samples

Sample	Lithology	Porosity (%)	Permeability (mD)	Dry density (g/cm^3)	Clay content (%)
A	Muddy Siltstone	2.88	0.0045	2.61	2.8
B	Muddy Siltstone	4.6	0.38	2.56	8.2
C	Siltstone	5.2	0.019	2.58	1.9
D	Silty Mudstone	5.56	0.011	2.53	12.5
E	Siltstone	5.6	0.017	2.52	2.4
F	Siltstone	5.79	0.035	2.41	3.9
G	Siltstone	5.8	0.02	2.55	3
H	Siltstone	6.45	0.097	2.38	5.5
I	Siltstone	10.87	0.39	2.29	5.5
J	Muddy Siltstone	12.75	0.17	2.3	4.4
K	Siltstone	13.09	0.08	2.28	5.5
L	Siltstone	13.97	0.084	2.26	5.5

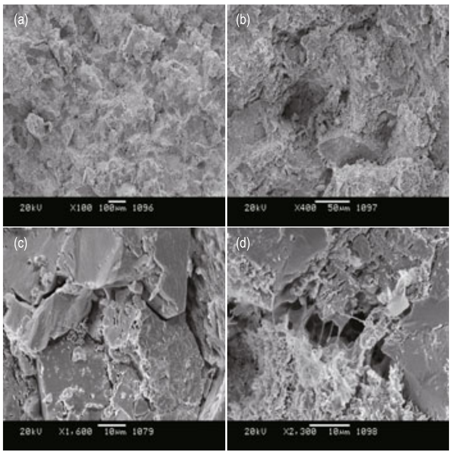

Fig. 1 SEM photographs of sample K at different magnifications: (a) closely arranged grains; (b) view of the rock surface, with intergranular pores; (c) grain contacts and microcracks; and (d) intergranular pores filled with illite (mud).

In tight oil reservoirs, the grain surfaces and pores are coated and filled by clay minerals (mud). The porosity is typically low. There are also grain contacts and grain dissolution cracks. Ba et al. (2016) proposed the double-porosity structure model in which clay minerals in intergranular pores are regarded as inclusions. In this study, we consider the skeleton with intergranular pores as the host skeleton, and the grain contact and microcracks and clay minerals as two different types of inclusions. The structure of tight oil reservoirs can be described by the triple-porosity medium model, as shown in Figure 2a. Thus, the rock matrix can be regarded as a complex combination of three homogeneous skeleton components, i.e., intergranular pores, microcracks, and clay minerals. The triple-porosity structure is shown in Figure 2b.

Data

The rock samples were cut into cylinders, 25 mm in diameter and 50–56 mm in length. The reference aluminum blocks were of the same shape and size. The rock samples were saturated with water, oil (kerosene), and gas (nitrogen) and the wave propagation velocities were measured at 80 °C, confining pressure of 50 MPa, and pore pressure of 25 MPa, i.e., the *in situ* conditions. The pulse frequency was approximately 1 MHz. The gas-saturated samples were first dried in an oven and then sealed with a rubber jacket in a high-pressure vessel. The confining pressure was increased to 50 MPa, and the pore pressure was set at 25 MPa by injecting nitrogen. We maintained the temperature at 80 °C for half an hour by heating the fluid in the vessel. Finally, the waveforms through the rock specimens were recorded. In the water-saturated and oil-saturated experimental measurements, the specimens were saturated with water and oil by depressurizing. The specimens were sealed and placed in a high-pressure vessel. The confining pressure was maintained at 50 MPa. Water or oil was injected to increase the pore pressure to 25 MPa, and then the specimens were heated at 80 °C for half an hour during the experiments.

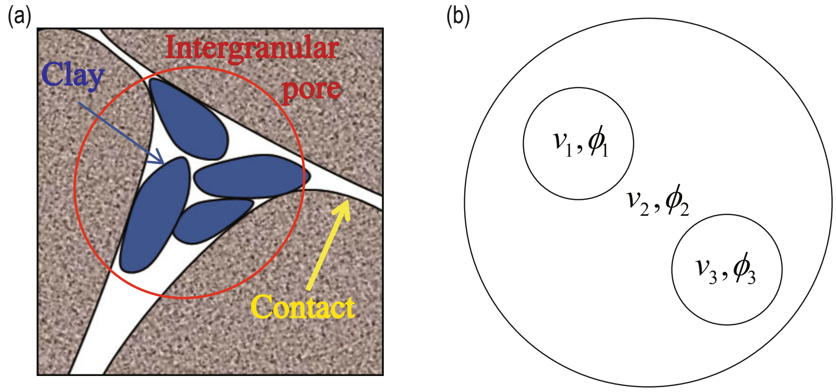

Fig. 2 Triple-porosity structure: (a) triple-porosity medium model with two kinds of inclusions and (b) volume ratio and absolute porosity of microcracks (v1 and φ1), host skeleton (v2 and φ2), and clay inclusions (v3 and φ3), where v1 + v2 + v3 = 1 and φ1 + φ2 + φ3 is the total porosity.

The P-wave velocity in sample K for different fluids and the reference aluminum rod are shown in Figure 3a. The P-wave attenuation is estimated by the spectral ratio method (Guo et al., 2009, Figure 3) as follows:

$$\ln\left(\frac{A_1(f)}{A_2(f)}\right) = \left(\frac{\pi x}{Q_2 V_2} - \frac{\pi x}{Q_1 V_1}\right) f + \ln\frac{G_1(x)}{G_2(x)}, \tag{1}$$

where f is the frequency and $A_1(f)$ and $A_2(f)$ are the P-wave spectra in the rock and aluminum cylinders, respectively; the quality factors of the rock specimens and aluminum rod are Q_1 and Q_2; the P-wave velocities of the sample and aluminum rod are V_2 and V_2; x is the travel path of the waves in the rock specimens and aluminum rod; $G(x)$ is a geometric factor related to the shape and size of the rock specimens.

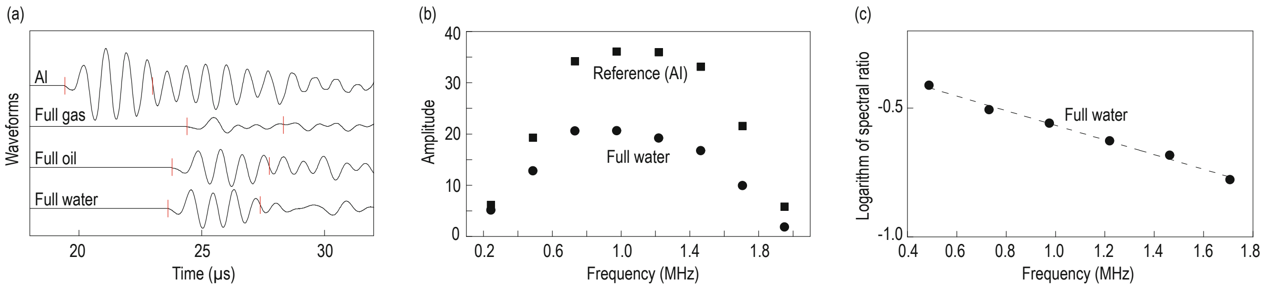

Fig. 3 Spectral ratio method of estimating P-wave attenuation in sample K: (a) P-waveforms through the reference (aluminum) and rock cylinders saturated with gas, oil, and water from top to bottom, the selected P-wave time window is between the red bars; (b) spectra calculation by the Fourier transform, the diagram shows the P-wave spectra of the aluminum and water-saturated specimen; and (c) logarithmic spectral ratios for estimating the quality factor Q.

To estimate the P-wave attenuation by the spectral ratio method, we first select the appropriate time window for the P-waveforms in the specimens and aluminum rod. The selected time window is four periods after the first arrival of the P-waves (Figure 3a). Then, the spectra of the corresponding waveforms are obtained using the fast Fourier transform and select the appropriate main frequency band (Figure 3b). assuming constant attenuation in the ultrasonic frequency band, the logarithmic spectral ratio of the selected frequency band should have good linear relation. We finally calculate the spectral ratio in the rock specimens and reference aluminum rod using least squares to fit the spectral ratio of the main frequency band and obtain the line slope (Figure 3c). Equation (1) is used to obtain the corresponding Q^{-1} at each frequency within the main frequency band.

Data analysis

The wave velocities and attenuation in gas-, water-, and oil-saturated specimens are calculated and then assessed. Figures 4a and 4b show that when the porosity increases from 2% to 14%, the P-wave velocities in the gas-saturated rocks decrease from 5095 to 3971 m/s, and the P-wave velocity differences between water- and gas-saturated specimens increase from 58 to 254 m/s. The S-wave velocity in the gas-saturated rock specimens decreases from 2763 to 2265 m/s, and the S-wave velocity difference between water- and gas-saturated specimens increase from 16 to 38 m/s. The results suggest that the fluid type in the pores affects the P-wave velocity more than the S-wave velocity. Figures 4c and 4d show that the relation between P-wave attenuation and porosity is not obvious, and P-wave attenuation at ultrasonic frequency increases with increasing permeability.

The attenuation in the gas-saturated specimens is higher than in oil- or water-saturated specimens. This differs from published data on P-wave attenuation in rocks. at ultrasonic frequency. Apparently, attenuation characteristic is related to the structural characteristics of each rock type.

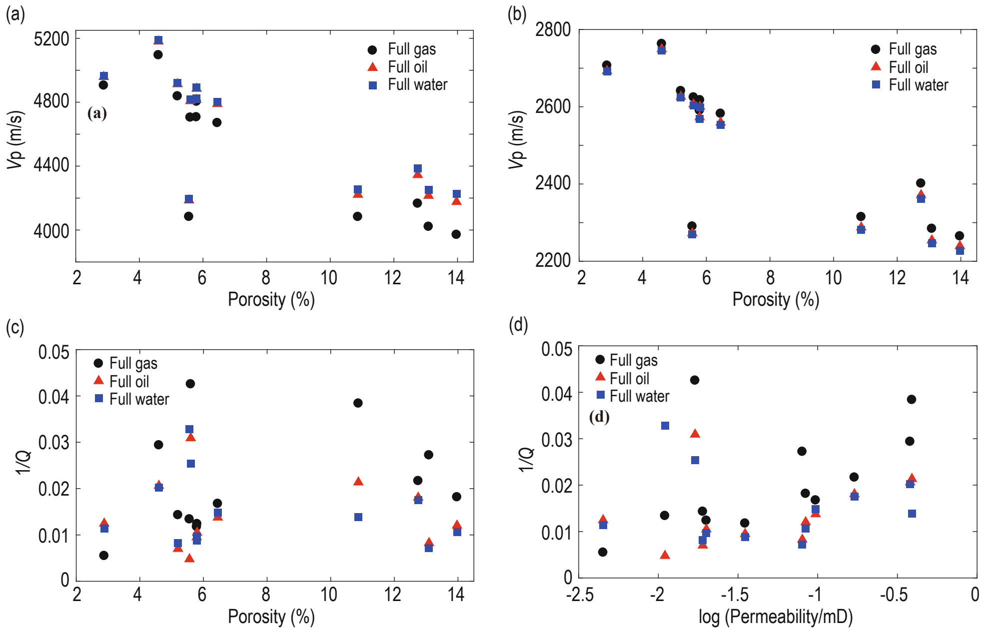

Fig. 4 (a) P-wave velocity vs porosity, (b) S-wave velocity vs porosity, (c) P-wave attenuation vs porosity, and (d) P-wave attenuation vs permeability.

The triple-porosity structure model

To assess the effect of fabric heterogeneity, it is necessary to establish a reasonable physical model of the seismic wave response and fluid flow characteristics. The Gassmann–Biot model (Gassmann, 1951; Biot, 1956) offers the basic theoretical framework for studying wave propagation in fluid–solid porous media. However, the model cannot be applied to complex heterogeneous media. Ba et al. (2011) derived a double-porosity medium model that combines the Biot and Rayleigh equations of fluid pocket oscillations to simulate the wave propagation in a heterogeneous double-porosity medium. Tight oil reservoirs have low porosity, extremely low permeability, and strong heterogeneity. The pore structure cannot be simplified as a single- or double-porosity structure at the microscopic scale. SEM observations suggest that there are grain contacts or microcracks in addition to intergranular pores and clay minerals in tight oil reservoirs. Therefore, tight oil reservoirs are best described by the triple-porosity structure model (Figure 2b).

The wave governing equations of triple-porosity medium model were derived based on Hamilton principle, which could describe the wave-induced local fluid flow in the triple-porosity structure reservoir (Zhang et al., 2017). By incorporating the local fluid flow interaction into the potential energy, kinetic energy and dissipated energy, the dynamic equations of elastic wave propagation were established. The dynamic equations can simulate the P-wave velocity dispersion and attenuation of tight oil reservoir with triple-porosity structure:

$$\begin{aligned} &N\nabla^2\mathbf{u}+(A+N)\nabla e+Q_1\nabla(\xi_1+\phi_2\zeta_{12})+Q_2\nabla(\xi_2-\phi_1\zeta_{12}+\phi_3\zeta_{23})+Q_3(\xi_3-\phi_2\zeta_{23}) \\ &=\rho_{00}\ddot{\mathbf{u}}+\rho_{01}\ddot{\mathbf{U}}^{(1)}+\rho_{02}\ddot{\mathbf{U}}^{(2)}+\rho_{03}\ddot{\mathbf{U}}^{(3)}+b_1\left(\dot{\mathbf{u}}-\dot{\mathbf{U}}^{(1)}\right)+b_2\left(\dot{\mathbf{u}}-\dot{\mathbf{U}}^{(2)}\right)+b_3\left(\dot{\mathbf{u}}-\dot{\mathbf{U}}^{(3)}\right), \end{aligned} \tag{2a}$$

$$Q_1\nabla e+R_1\nabla(\xi_1+\phi_2\zeta_{12})=\rho_{01}\ddot{\mathbf{u}}+\rho_{11}\ddot{\mathbf{U}}^{(1)}-b_1\left(\dot{\mathbf{u}}-\dot{\mathbf{U}}^{(1)}\right), \tag{2b}$$

$$Q_2\nabla e+R_2\nabla(\xi_2-\phi_1\zeta_{12}+\phi_3\zeta_{23})=\rho_{02}\ddot{\mathbf{u}}+\rho_{22}\ddot{\mathbf{U}}^{(2)}-b_2\left(\dot{\mathbf{u}}-\dot{\mathbf{U}}^{(2)}\right), \tag{2c}$$

$$Q_3\nabla e+R_3\nabla(\xi_3-\phi_2\zeta_{23})=\rho_{03}\ddot{\mathbf{u}}+\rho_{33}\ddot{\mathbf{U}}^{(3)}-b_3\left(\dot{\mathbf{u}}-\dot{\mathbf{U}}^{(3)}\right), \tag{2d}$$

$$\begin{aligned} &\frac{1}{3}\rho_f R_{12}^2\ddot{\zeta}_{12}\phi_2^2\phi_1\left(\frac{1}{5}+\frac{\phi_{10}}{\phi_{20}}\right)+\frac{1}{3}\left(\frac{\eta}{5\kappa_1}+\frac{\eta}{\kappa_2}\right)R_{12}^2\dot{\zeta}_{12}\phi_2^2\phi_1\phi_{10} \\ &=\phi_2\left(Q_1e+R_1(\xi_1+\phi_2\zeta_{12})\right)-\phi_1\left(Q_2e+R_2(\xi_2-\phi_1\zeta_{12}+\phi_3\zeta_{23})\right), \end{aligned} \tag{2e}$$

$$\begin{aligned} &\frac{\phi_3}{3}\rho_f R_{23}^2\ddot{\zeta}_{23}\phi_2^{2}\left(\frac{1}{5}+\frac{\phi_{30}}{\phi_{20}}\right)+\frac{1}{3}\left(\frac{\eta}{\kappa_2}+\frac{\eta}{5\kappa_3}\right)R_{23}^2\dot{\zeta}_{23}\phi_2^{2}\phi_3\phi_{30} \\ &=\phi_3\left(Q_2e+R_2(\xi_2-\phi_1\zeta_{12}+\phi_3\zeta_{23})\right)-\phi_2\left(Q_3e+R_3(\xi_3-\phi_2\zeta_{23})\right). \end{aligned} \tag{2f}$$

where parameter **u** donates the displacement of solids. the absolute velocity vector of the solids, microcracks, intergranular pores, clays, and pore fluid are $\dot{\mathbf{u}}$ and $\dot{\mathbf{U}}^{(1)},\dot{\mathbf{U}}^{(2)},\dot{\mathbf{U}}^{(3)}$, respectively. Parameters e,ζ_1, ζ_2,ζ_3 denote the displacement divergence of solids and fluids in the three types of pores. The scalars ζ_{12},ζ_{13} denote the variations in fluid content owing to the local fluid flow between microcracks and intergranular pores and that between clays and intergranular pores, respectively. The stiffness coefficients $A,N,Q_1,Q_2,Q_3,R_1,R_2,R_3,$ the dissipation coefficients $b_1,b_2,b_3,$ and the density parameters $\rho_{00},\rho_{01},\rho_{02},\rho_{03},\rho_{11},\rho_{22},\rho_{33},$ all depend on rock properties. Parameters $k_1,k_2,k_3,$ denote the permeability of the microcrack skeleton, the host skeleton, and the clay minerals skeleton, respectively. Parameters $R_{12},R_{23},$ denote the radii of microcracks and clay minerals. The volume ratio and porosity of microcracks are $v_1,\phi_{10},$ the volume ratio and porosity of the host skeleton are $v_2,\phi_{20},$ and the volume ratio and absolute porosity of clay inclusions are $v_3,\phi_{30},$ respectively. Parameters $\phi_1,\phi_2,\phi_3,$ denote the absolute porosities of microcracks, host skeleton, and clay inclusions, respectively, where the sum of $\phi_1,\phi_2,\phi_3,$ is the total porosity. Parameters $\rho_f,\eta,$ denote the fluid density and viscosity, respectively.

We performed plane-wave analysis by substituting the plane-wave analytical kernel into equations (2a)–(2f) to predict the wave velocity and attenuation (Ba et al., 2011).

Pore structure and P-wave propagation

To model the P-wave velocity dispersion and attenuation in tight oil reservoirs, the triple-porosity structure model parameters are set on the basis of the physical parameters of sample K. The bulk and shear moduli are obtained by the Gassmann equation using the P- and S-wave velocities of the gas-saturated specimens. The porosity, permeability, and grain density are obtained experimentally. The pore fluid parameters are calculated by the Batzle–Wang (1992) equations. The densities of gas, oil, and water are 0.3, 0.79, and 0.98 g/cm^3; the bulk moduli are 0.031, 1.27, and 2.53 GPa; and the gas, oil, and water viscosities are 0.031, 2.1, and 0.35 cP, respectively. We simulate the P-wave velocity dispersion and attenuation by adjusting the pore structure parameters within a reasonable range. The parameters are listed in Table 2.

Table 2. Triple-porosity structure model parameters based on sample K

Bulk modulus (GPa)	Porosity	Dry density (g/cm^3)	Microcrack radius (μm)	Microcrack volume ratio	Microcrack porosity	Clay radius (μm)	Clay volume ratio	Clay inclusion porosity
40	0.1309	2.625	25/ 50/ 100	0.001/ 0.005/ 0.01	0.05/ 0.1/ 0.15	5/ 10/ 25	0.001/ 0.005/ 0.01	0.005/ 0.01/ 0.1

Figure 5 shows the effect of microcrack radius on P-wave velocity dispersion and attenuation. With increasing microcrack radius, the velocity dispersion steps and attenuation peaks at low frequencies shift to even lower frequencies. However, the velocity dispersion steps and attenuation peaks at high frequencies do not change. The dispersion steps and attenuation peaks shift to the low frequency end with increasing fluid viscosity. The change in the microcrack radius only affects the attenuation peak frequency and has no effect on the attenuation peak magnitude.

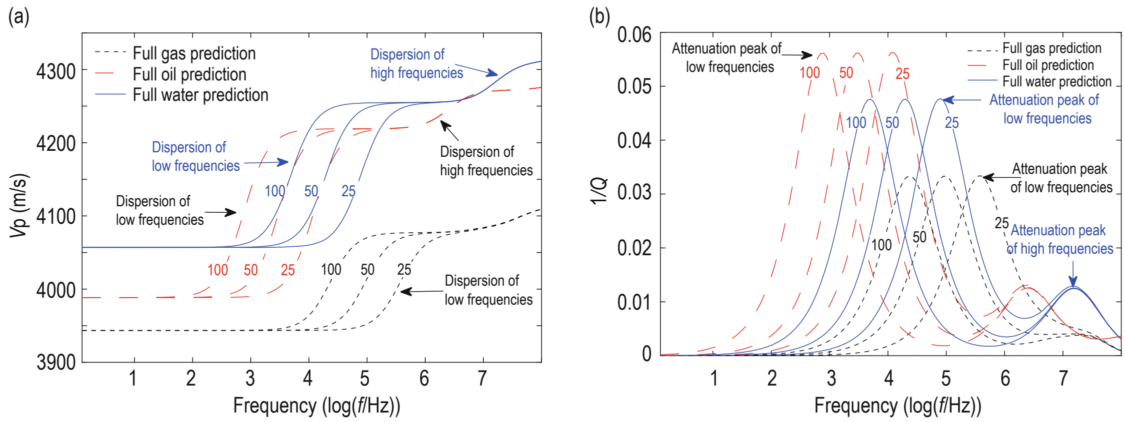

Fig. 5 Effect of microcrack radius on (a) P-wave velocity dispersion and (b) attenuation in tight oil reservoirs. The microcrack radii are 25, 50, and 100 μm.

Figure 6 shows the effect of clay inclusions radius on the P-wave velocity dispersion and attenuation in tight oil reservoirs. With increasing inclusion radius, the velocity dispersion steps and attenuation peaks at high frequencies shift to lower frequencies and gradually overlap with the dispersion steps and attenuation peaks at the low frequency end. However, the degree of dispersion of the P-wave velocity does not change when the clay inclusion radius increases. The attenuation peak after superposition is the highest when the characteristic frequencies of two attenuation peaks are the same.

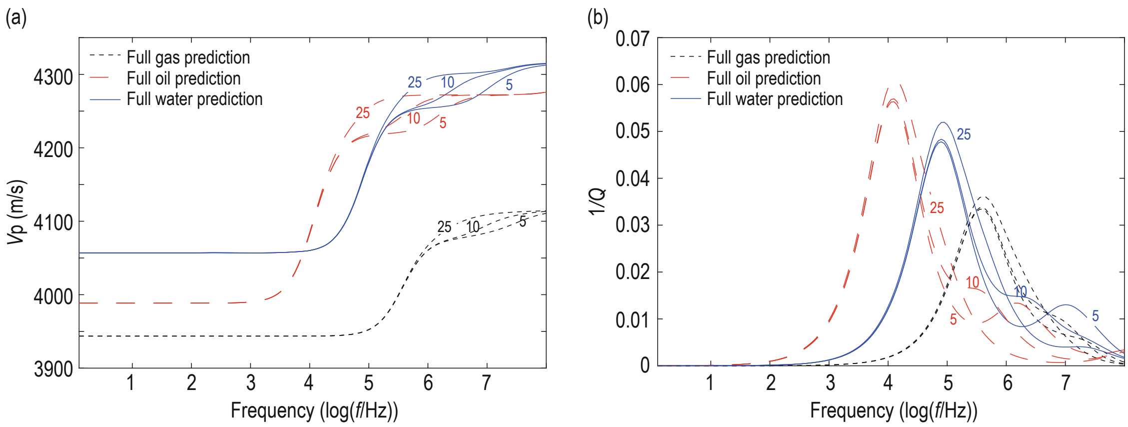

Fig. 6 Effect of clay (mud) radius on (a) P-wave velocity dispersion and (b) attenuation. The clay minerals radii are 5, 10, and 25 μm.

Figure 7 shows the effect of microcrack volume ratio on the P-wave velocity dispersion and attenuation. The degree of velocity dispersion intensifies at low frequencies, and the corresponding attenuation peaks increase with increasing microcrack volume ratio. In addition, the attenuation peaks at low frequencies gradually increase and shift to higher frequencies. The attenuation intensifies because of the local fluid flow between microcracks and intergranular pores when the microcrack volume increases. However, the attenuation peaks at relatively high frequencies gradually decrease and shift toward high frequencies. The local fluid flow between clay inclusions and intergranular pores weakens owing to the reduction in the host skeleton volume.

Figure 8 shows the effect of clay inclusions volume ratio on P-wave velocity dispersion and attenuation.

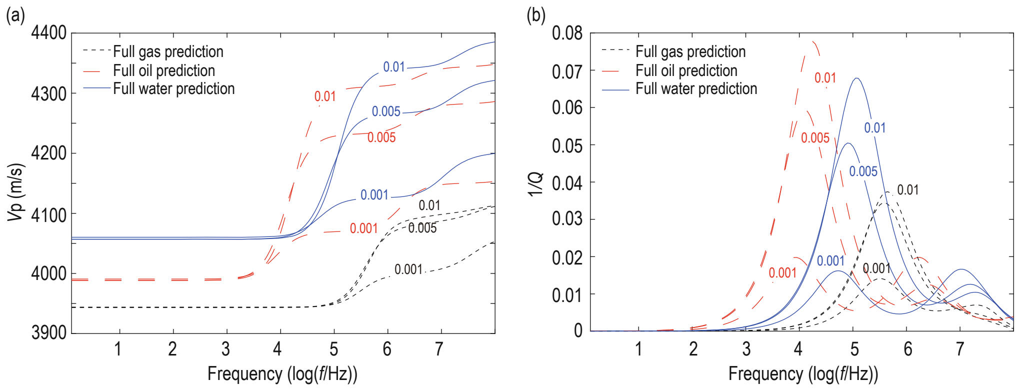

Fig. 7 Effect of microcrack volume ratio on (a) P-wave velocity dispersion and (b) attenuation. The microcrack volume ratios are 0.001, 0.005, and 0.01.

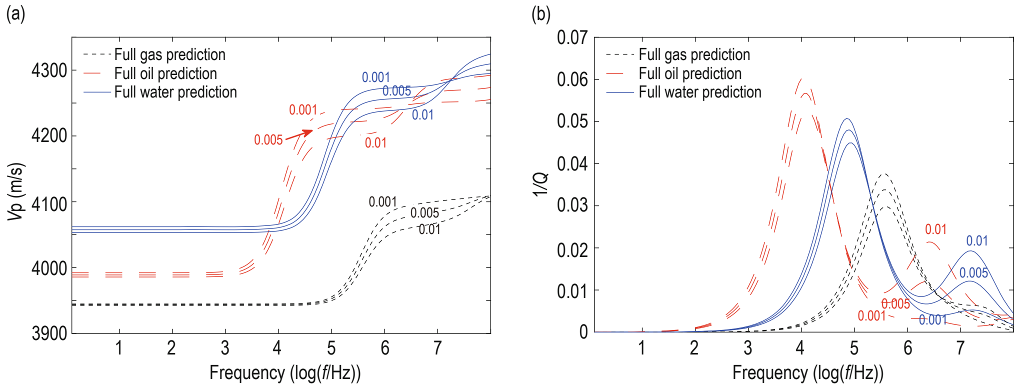

Fig. 8 Effect of clay inclusions volume ratio on (a) P-wave velocity dispersion and (b) attenuation. The clay inclusions volume ratios are 0.001, 0.005, and 0.01.

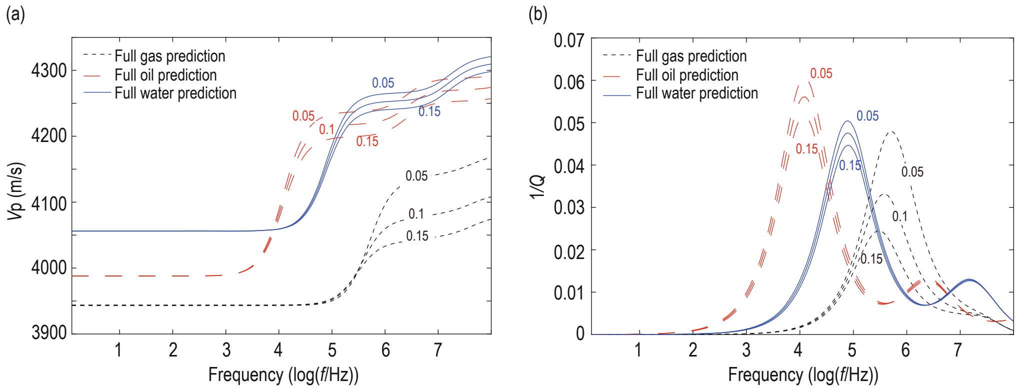

Fig. 9 Effect of microcrack porosity on (a) P-wave velocity dispersion and (b) attenuation. Microcrack porosities are 0.05, 0.1, and 0.15.

With increasing clay inclusions volume ratio, velocity dispersion increases at relatively high frequencies as well as the attenuation peaks but with a small decrease at the lower frequencies. This is attributed to the strong local fluid flow between clay minerals and intergranular pores.

Figures 9 and 10 show the effects of microcracks and mud porosities on P-wave velocity dispersion and attenuation, respectively. With increasing microcrack porosity, dispersion decreases at low frequencies. The corresponding attenuation peaks decrease, whereas the attenuation peaks at high frequencies do not change. Only the velocity dispersion and attenuation peak at high frequency are affected with changing clay porosity.

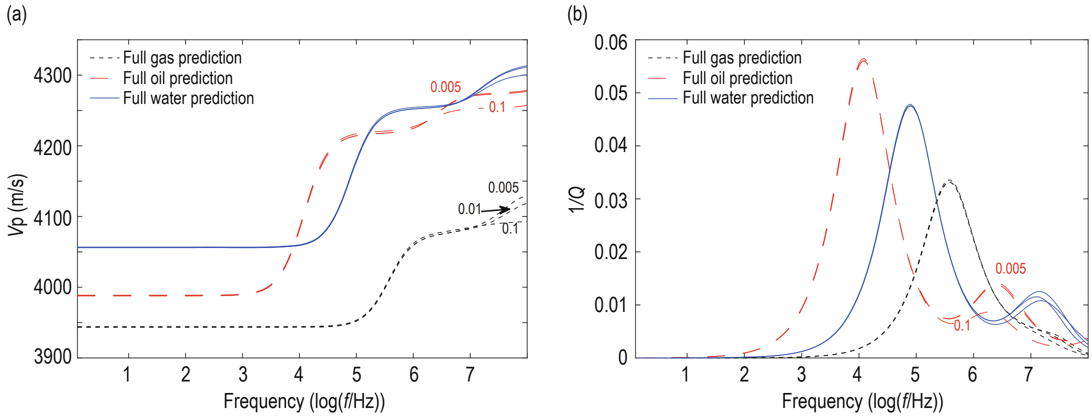

Fig. 10 Effect of clay (mud) porosity on (a) P-wave velocity dispersion and (b) attenuation. Mud porosities are 0.005, 0.01, and 0.1.

P-wave velocity and attenuation and fluids

We assess the velocity dispersion and attenuation in the specimens saturated with different fluid types by using the Biot model, the Biot–Rayleigh double-porosity medium model, and the triple-porosity medium model. The bulk and shear moduli were determined by the Gassmann equation using the measured P- and S-wave velocities at gas saturation. The P-wave velocity and attenuation were measured by adjusting the bulk moduli, radii, and volume ratios of microcracks and clays. The modeling parameters for sample K are listed in Table 3. The predicted and experimental results are shown in Figures 11 and 12.

Table 3. Biot Model and Biot–Rayleigh Model considering one kind of inclusions

Bulk modulus (GPa)	Dry density (g/cm^3)	Porosity	Host skeleton permeability (mD)	Inclusion volume ratio	Inclusion porosity	Inclusion radius (μm)
40	2.625	0.1309	0.08	0.004	0.1	23

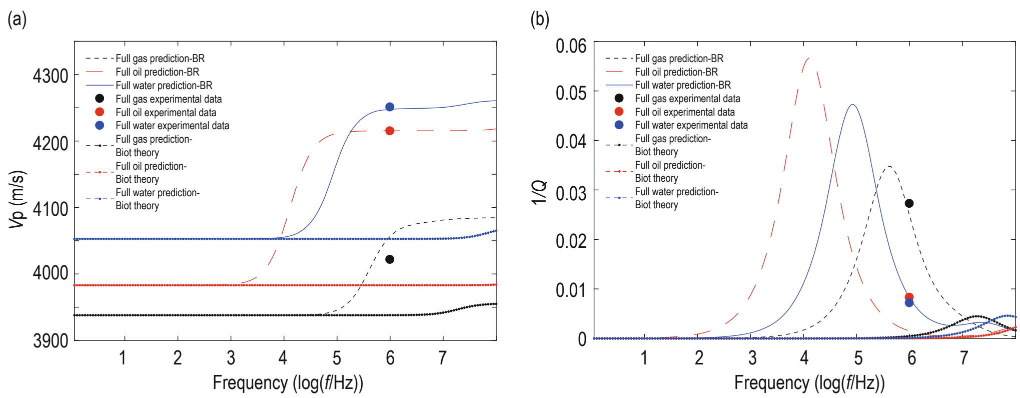

Fig. 11 (a) P-wave velocity dispersion and (b) attenuation predicted by the Biot and Biot–Rayleigh models.

Figure 11 shows that the Biot model underestimate the experimental P-wave velocities and attenuation data. Because the Biot model only considers macroscopic fluid flow in rocks, the dissipation caused by fluid oscillation is very weak. The P-wave velocities predicted by the Biot–Rayleigh model well match the experimental data, and the P-wave velocity data coincide with the Biot model at the low frequency limit. However, the attenuation predicted by the Biot–Rayleigh model suggests that the attenuation in oil-saturated specimens is low at 1 MHz and does not match the experimental attenuation data of sample K. Figure 12 shows the experimental P-wave velocities and attenuation and those predicted by the triple-porosity structure model. Clearly, there is good agreement between the two. The attenuation in gas-saturated specimens is stronger than in water- or oil-saturated specimens owing to the difference in the attenuation frequency and viscosity of the fluids. The P-wave velocity dispersion in the fluid-saturated specimens show the inflection points of velocity dispersion shift to lower frequencies with increasing fluid viscosity, i.e., gas, water, and oil. The triple-porosity structure model also predicts two attenuation peaks.

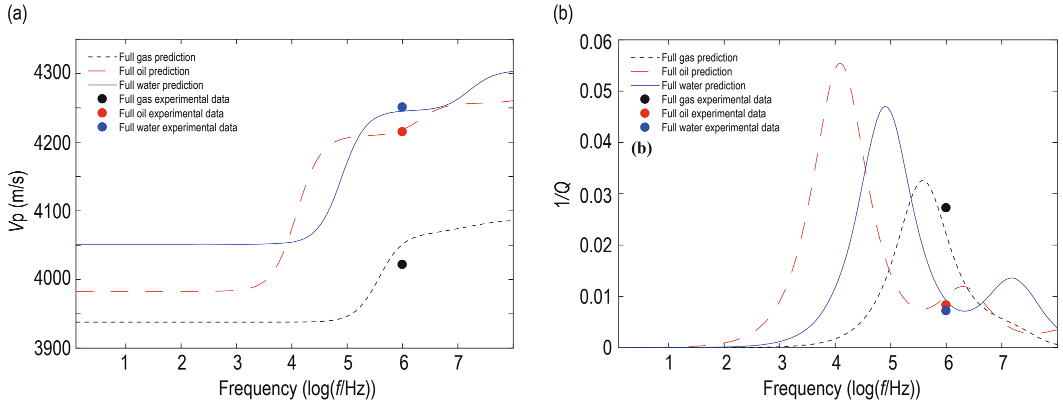

Fig. 12 Triple-porosity structure model: (a) P-wave velocity dispersion and (b) attenuation.

Figures 13 and 14 compare the agreement between the triple-porosity structure model and experimental P-wave velocity and attenuation. Clearly, the model could be used to infer the physical properties of tight oil reservoirs.

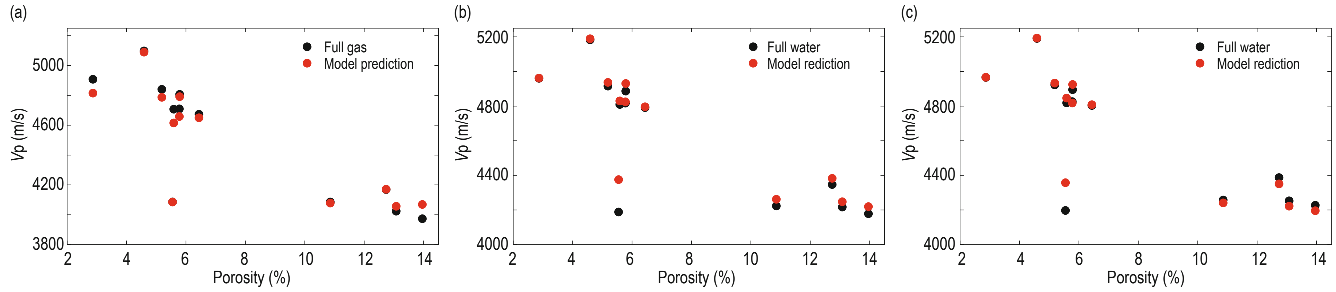

Fig. 13 Triple-porosity structure model vs experimental P-wave velocity.

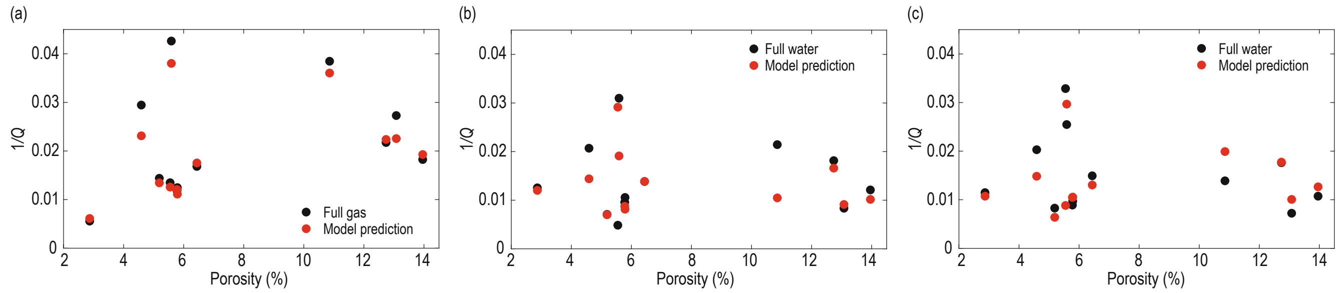

Fig. 14 Triple-porosity structure model vs experimental P-wave attenuation.

Physical properties

The experimental P-wave velocity (V_p) and attenuation (Q^{-1}) at gas, oil, and water saturation are used to determine the microcrack volume ratio (v_1), clay volume ratio (v_3), microcrack radius (R_{12}), clay radius (R_{23}), microcrack bulk modulus (K_{b1}), and clay bulk modulus (K_{b3}) of the rock samples by inversion. On the basis of model parameters, the pore structure is analyzed. The microcrack bulk modulus denotes the compressibility of the inclusions, and the microcrack radius reflects the heterogeneity of the pore structure. As shown in Figure 15, the relation between microcrack bulk modulus and porosity suggests that large-radius microcracks are less compressible with increasing porosity, whereas the compressibility of small-radius microcracks is the opposite, suggesting that in tight oil reservoirs, increased porosity may be associated with large microcracks.

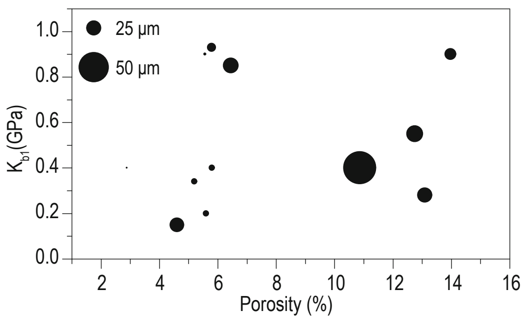

Fig. 15 Microcrack bulk modulus vs porosity; the circle size represents the microcrack radius.

It can be seen from Figure 16 that the P-wave attenuation, microcrack radius, and permeability are positively correlated at gas saturation conditions. The microcrack radius gradually increases with increasing permeability. The P-wave attenuation is also high in gas-saturated specimens. The connectivity between the microcracks is better when the microcrack size is large.

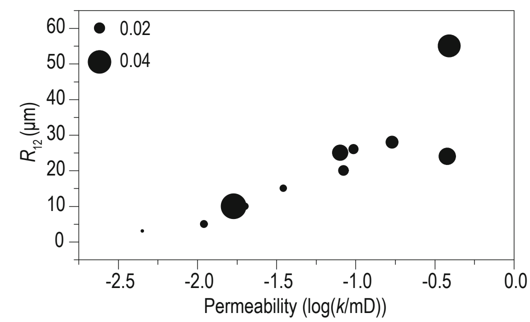

Fig. 16 Microcrack radius vs permeability; the circle size represents the attenuation in the gas-saturated specimens.

This enhances the local fluid flow between pores and microcracks, resulting in stronger P-wave attenuation.

The clay bulk modulus and radius gradually increase with increasing porosity in Figure 17. Thus, it is inferred that clay inclusions have typically high radius and low compressibility in tight oil reservoirs with relatively high porosity.

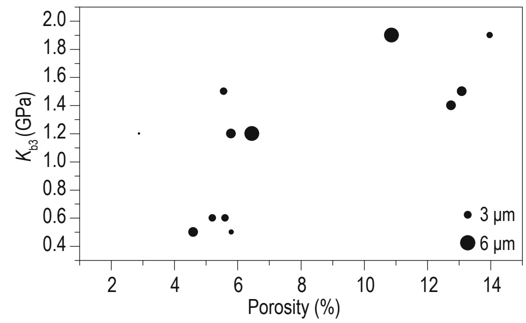

Fig. 17 Clay inclusions bulk modulus vs porosity; the circle size represents the radius of the inclusions.

Figure 18 shows the average grain size and standard deviation in six of the specimens. The standard deviation reflects the sorting of mineral grains. The smaller the standard deviation is, the better the sorting and the more uniform the mineral grains are. In six of the specimens, the grain diameters are between 0.027 and 0.043 mm. The standard deviation is between 1.55 and 1.85, suggesting poor sorting. With increasing average grain size, the standard deviation decreases, whereas the microcrack radius increases. The distribution of mineral grain is more uniform with increasing grain size. The microcrack radius is small because the pores between large grains are not filled by fine grains.

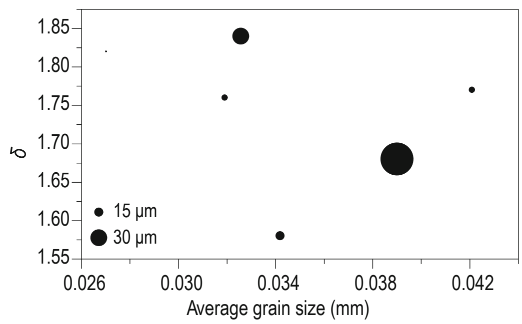

Fig. 18 Standard deviation vs average grain diameter in six of the specimens; the circle size represents the microcrack radius.

To evaluate the physical properties of the tight oil reservoirs in the Qingshankou Formation of the Daqing Oilfield, we classified the 12 samples into three groups based on porosity: porosity <5%, porosity 5–10%, and porosity >10%. Figure 19 shows that with increasing porosity, the P-wave velocity decreases, whereas the attenuation increases at gas saturation conditions. The microcrack volume ratio is the highest at porosity of 5–10%, but overall it does not change significantly with increasing porosity. The clay volume ratio increases with increasing porosity. When the porosity is less than 10%, the microcrack radius changes little; however, for porosity >10%, the microcrack radius increases rapidly. The clay inclusion radius increases with increasing porosity, but the variation is small. This suggests that at high porosity, the microcracks and clay inclusions in the rock samples are large. The microcrack radius is significantly larger than the mud radius, consistent with the SEM observations. The microcrack bulk modulus is the highest at porosity of 5–10%, meaning that the microcrack compressibility is low. The clay inclusion bulk modulus is higher than the microcrack bulk modulus and increases with increasing porosity. Apparently, the compressibility of clay inclusions in tight oil reservoirs is lesser than that of microcracks.

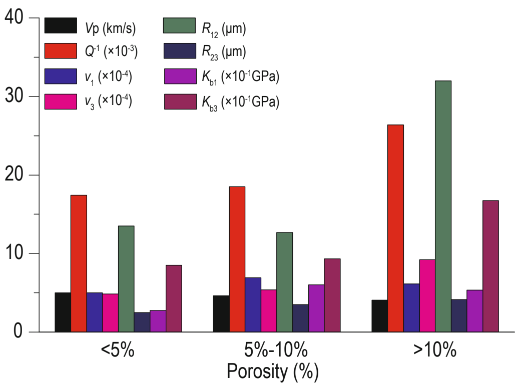

Fig. 19 Histograms of P-wave velocity (V_p), attenuation (Q^{-1}), microcrack volume ratio (v_1), clay volume ratio (v_3), microcrack radius (R_{12}), clay radius(R_{23}), microcrack bulk modulus (K_{b1}), and clay bulk modulus (K_{b3}) in the rock specimens.

Conclusions

The attenuation characteristics of tight oil reservoir samples saturated with different fluids were evaluated on the basis of ultrasonic experiments. The results suggest that at ultrasonic frequencies, the P-wave attenuation is stronger in gas-saturated samples than in oil- or water-saturated ones. The attenuation increases with increasing permeability.

The triple-porosity structure model of the P-wave velocity dispersion and attenuation suggests that there are possibly two dispersion inflection points that correspond to two attenuation peaks. The attenuation peak frequencies decrease with increasing fluid viscosity.

Modeling of the P-wave velocity and attenuation suggests that the triple-porosity structure model yields better results than the Biot and Biot–Rayleigh models. The attenuation is attributed to wave-induced local fluid flow because of microcracks and clay inclusions.

The Qingshankou Formation samples contain more clay inclusions and larger microcracks in the high porosity range; moreover, the compressibility and radii of the clay inclusions are smaller than those of the microcracks, whereas the volume ratios of both are similar.

The attenuation is modeled considering the heterogeneities in the microcracks and submicroscopic clay inclusions. Mesoscopic heterogeneities (10^{-4}–10^{-2} m) may result in stronger attenuation peaks in the sonic or seismic frequency band in heterogeneous reservoirs. This phenomenon cannot be observed in the ultrasonic data; however, models can help explain and describe the attenuation characteristics in the low frequency band, including seismic frequencies, by considering large-scale heterogeneous inclusions.

References

Adam, L., Batzle, M., Lewallen, K. T., and Van Wijk, K., 2009, Seismic wave attenuation in carbonates: Journal of Geophysical Research: Solid Earth, 114, B06208.

Agersborg, R., Johansen, T. A., Jakobsen, M., et al., 2008, Effects of fluids and dual-pore systems on pressure-dependent velocities and attenuations in carbonates: Geophysics, **73**, N35–N47.

Ba, J., Carcione J. M., and Nie, J. X., 2011, Biot-Rayleigh theory of wave propagation in double-porosity media: Journal of Geophysical Research: Solid Earth, **116**, B06202.

Ba, J., Zhao, J. G., Carcione J. M., and Huang, X. X., 2016, Compressional wave dispersion due to rock matrix stiffening by clay squirt flow: Geophysical Research Letters, **43**, 6186–6195.

Batzle, M. L., and Wang, Z., 1992, Seismic properties of pore fluids: Geophysics, **57**, 1396–1408.

Berryman, J. G., and Milton, G. W., 1991, Exact results for generalized Gassmann equations in composite porous-media with two constituents: Geophysics, **56**(12), 950–1960.

Best, A. I., and Sams, M. S., 1997, Compressional wave velocity and attenuation at ultrasonic and sonic frequencies in near-surface sedimentary rocks: Geophysical Prospecting, **45**, 327–344.

Biot, M. A., 1956, Theory of propagation of elastic waves in fluid-saturated porous solid. I. Low-frequency range: Journal of the Acoustical Society of America, **28**, 168–178.

Borgomano, J. V. M., Pimienta, L., Fortin, J., and Guéguen Y., 2017, Dispersion and attenuation measurements of the elastic moduli of a dual-porosity limestone: Journal of Geophysical Research: Solid Earth, **122**, 2690–2711.

Chapman, S., Tisato, N., Quintal, B., and Holliger K., 2016, Seismic attenuation in partially saturated Berea sandstone submitted to a range of confining pressures: Journal of Geophysical Research: Solid Earth, **12**1, 1664–1676.

Gassmann, F., 1951, Über die Elastizität poröser Medien: Vierteljahrsschrift der Naturforschenden Gesellschaft in Zürich, **96**, 1–23.

Guo, M. Q., Fu, L. Y., and Ba, J., 2009, Comparison of stress-associated coda attenuation and intrinsic attenuation from ultrasonic measurements: Geophysical Journal International, **178**, 447–456.

He, T., Zou, C. C., Pei, F. G., et al., 2010, Laboratory study of fluid viscosity induced ultrasonic velocity dispersion in reservoir sandstones: Applied Geophysics, **7**(2), 114–126.

Huang, W. B., Hersi, O. S., Lu, S. F., and Deng, S. W., 2017, Quantitative modelling of hydrocarbon expulsion and quality grading of tight oil lacustrine source rocks: Case study of Qingshankou 1 member, central depression, Southern Songliao Basin, China: Marine and Petroleum Geology, **84**, 34–48.

Johnston, D. H., Toksöz, N. M., and Timur, A., 1979, Attenuation of seismic waves in dry and saturated rocks: II. Mechanisms: Geophysics, **44**, 691–711.

Johnston, D. H., and Toksöz, M. N., 1980, Ultrasonic P and S wave attenuation in dry and saturated rocks under pressure: Journal of Geophysical Research: Solid Earth, **85**, 925–936.

Kuteynikova, M., Tisato, N., Jänicke, R., and Quintal B., 2014, Numerical modeling and laboratory measurements of seismic attenuation in partially saturated rock: Geophysics, **79**, L13–L20.

Marín-Moreno, H., Sahoo, S. K., and Best A. I.,2017, Theoretical modeling insights into elastic wave attenuation mechanisms in marine sediments with pore-filling methane hydrate: Journal of Geophysical Research: Solid Earth, **122**,1835–1847.

Oh, T. M., Kwon, T. H., Cho, G. C., 2011, Effect of partial water saturation on attenuation characteristics of low porosity rocks: Rock Mechanics and Rock Engineering, **44**(2), 245–251.

Pride, S. R., and Berryman, J. G., 2003a, Linear dynamics of double-porosity and dual-permeability materials. I. Governing equations and acoustic attenuation: Physical Review E, **68**, 036603.

Pride, S. R., and Berryman, J. G., 2003b, Linear dynamics of double-porosity and dual permeability materials. II. Fluid transport equations: Physical Review E, **68**, 036604.

Sams, M. S., Neep, J. P., and Worthington, M. H., 1997, The measurement of velocity dispersion and frequency-dependent intrinsic attenuation in sedimentary rocks: Geophysics, **62**, 1456–464.

Sayar, P., and Torresverdín, C., 2017, Effective medium modeling of velocity dispersion and attenuation in isotropic rocks: Geophysics, **82**(2), D135–D156.

Shi, L. Z., Wang, Z. Z., Zhang, G., et al., 2015, Distribution and formation of tight oil in Qijia area, Songliao Basin, NE China: Petroleum Exploration and Development, 42(1), 48–55.

Spencer, J. W., Shine, J., 2016, Seismic wave attenuation and modulus dispersion in sandstones: Geophysics, **81**, D211–D231.

Toksöz, M. N., Johnston, D. H., and Timur, A., 1979, Attenuation of seismic waves in dry and saturated rocks: i. laboratory measurements: Geophysics, **44**, 681–690.

Winkler, K., 1985, Dispersion analysis of velocity and attenuation in Berea sandstone: Journal of Geophysical Research, **90**, 6793–6800.

Winkler, K., and Nur, A., 1979, Pore fluids and seismic attenuation in rocks: Geophysical Research Letters, **6**, 1–4.

Yang, K., Xiao, J., Wang, Y., and Ning, X., 2017, A Study on Qingshankou Formation's Tight Oil Characteristics and Accumulation mode in the northern Songliao Basin: Acta Sedimentologica Sinica, **35**(3), 600–610.

Zhang, L., Ba, J., Yin, W., et al., 2017, Seismic wave propagation equations of conglomerate reservoirs: A triple-porosity structure model: Chinese Journal of Geophysics (in Chinese), **60**(3), 1073–1087.

Ma Ru-Peng received his B.S. in Geological Engineering from Hohai University in 2016. He is presently a Ph.D. student in the School of Earth Sciences and Engineering at Hohai University. His research interests are rock physics and wave velocity dispersion and attenuation in porous media.

中文摘要

井旁裂缝对偶极横波反射波幅度影响分析//Influence of rock fractures on the amplitude of dipole-source reflected shear wave, 王浩[1]，李宁[1,2]，王才志[1]，武宏亮1，刘鹏[1]，李雨生[1,3]，刘英明[1], 原野[1], **APPLIED GEOPHYSICS**, **16**(1), P. 1−13. DOI:10.1007/s11770-019-0757-2

(1中国石油勘探开发研究院，北京 100083；2长江大学，湖北武汉 430100；3北京大学地球与空间科学学院，北京 100871)

摘要：在利用偶极横波反射波测井技术进行井旁裂缝识别中，横波反射波幅度受仪器声源辐射、井孔条件以及地层中偶极横波反射波衰减等因素的影响。在本文中，为了分析不同类型地层中井旁裂缝对横波反射波幅度的影响，我们首先利用偶极声场积分的远场渐进解和偶极声源辐射指向公式研究了快速、中速以及慢速地层中偶极声源的横波远场辐射性能和辐射指向；然后采用三维有限差分算法研究了横波反射波绝对幅度和相对幅度比值（反射波幅度与直达波幅度比值，RA）随裂缝参数变化的响应特征；最后利用RA分析了仪器在不同类型地层中的裂缝识别能力。结果表明：慢速地层中SH波的覆盖 特性和辐射波幅均弱于快速和中速地层，其反射波绝对幅度也相应较低，但其RA与快速和中速地层较为接近甚至更高，表明偶极横波测井仪器在慢速地层具有与快速和中速地层相同甚至更好的裂缝识别能力。此外，当RA较小时，不同类型地层中RA与各项裂缝参数之间均具有较好的相关性，可以作为确定反射波测井识别裂缝参数下限的依据。

关键词：偶极声源，反射横波，辐射特性，裂缝参数

岩石基质模量与临界孔隙度的联合预测方法//Simultaneous prediction of rock matrix modulus and critical porosity, 李诺[1,2,3], 陈浩*[1,2,3], 张秀梅[1,3], 韩建强[1,3], 王健[1,3], 王秀明[1,2,3], **APPLIED GEOPHYSICS**, **16**(1), P. 14–24. DOI:10.1007/s11770-019-0756-3

(1 中国科学院声学研究所声场与声信息国家重点实验室, 北京 100190；2 中国科学院大学, 北京100049; 3 北京市海洋深部钻探测量工程技术研究中心, 北京 100190)

摘要：岩石的基质模量和临界孔隙度是岩石物理模型的两项重要输入参数，但临界孔隙度通常很难获得。本文基于有效体积模量与孔隙度的线性模型，提出一种快速计算基质模量和临界孔隙度的方法。通过对实验室或现场测量的有效体积模量与孔隙度数据进行最小二乘拟合，利用拟合系数即可计算基质模量和临界孔隙度。本文方法适用的样品孔隙度范围广，并且计算结果能够准确反映样品的粘土含量、压力大小和饱和状态的差异。粘土含量高的样品的基质模量低，临界孔隙度小。压力对基质模量影响不大，但是临界孔隙度会随着压力的升高而略微增大。饱和样品计算得到的基质模量要比干燥的更大。

关键词：模量、孔隙度、粘土含量、压力、饱和度

利用LAMB波进行深水隔水管气侵早期监测//Early monitoring of gas influx of drilling fluid in risers during deepwater drilling using Lamb waves, 段文星，肖承文，艾勇，信毅，朱雷，**APPLIED GEOPHYSICS**, 2019, **16**(1), P. 25−32. DOI: 10.1007/S11770-019-0753-6

(中国石油塔里木油田勘探开发研究院，新疆 库尔勒 841000)

摘要：深水钻井隔水管气侵早期监测，对及时发现井中气体渗流，减少深水钻井中井喷事故，具有重要的意义。在本文中，我们对在深水隔水管内为水基钻井液的情况下，通过改变钻井液的含气率，利用三维柱坐标系有限差分方法数值模拟了声源在隔水管外表面激发的声场，分析了隔水管内A0 模式和S0 模式LAMB 波的幅度和衰减与管内流体性质以及段塞流顶底界面位置之间的关系。模拟结果表明，LAMB 波的幅度和衰减对低含气量非常敏感，能够反映隔水管内气体的含量，同时，有效地反映段塞流顶底界面的位置。

关键词：深水钻井，LAMB 波，隔水管，气侵

致密油岩石纵波频散及衰减特征研究：实验观测及理论模拟//Dispersion and attenuation of compressional waves in tight oil reservoirs:Experiments and simulations, 马汝鹏[1]，巴晶*[1]，Caarcione, J. M.[1,2]，周欣[1]，李帆[1]，**APPLIED**

GEOPHYSICS, 2019, 16(1), P. 33–45. DOI:10.1007/S11770-019-0748-3
(1. 河海大学地球科学与工程学院，地球探测研究所，南京211100；2. 2. Istituto Nazionale di Oceanografia e di Geofisica Sperimentale (OGS), Borgo Grotta Gigante 42c, Sgonico, Trieste 34010, Italy)

摘要：非常规油气资源-致密油在中国有广泛分布，致密油储层孔隙类型多样、结构复杂。本文对12块致密油岩石样本开展了超声波实验测量，根据记录的纵波波形，利用谱比法估算了岩石在饱和不同流体时的衰减，结果显示大部分致密油样本在饱气状态下的纵波衰减强于饱水及饱油情况，并且，纵波衰减与岩石渗透率有较好的正相关性。基于扫描电镜分析结果，采用三重孔隙结构模型描述致密油岩石，正演模拟了致密油岩石的波传播特征。基于BIOT理论、BIOT-RAYLEIGH双重孔隙介质理论和三重孔隙模型对比讨论了致密油岩石的纵波速度频散和衰减规律，结果显示BIOT理论和BIOT-RAYLEIGH理论均无法解释该组致密油岩石样本的衰减特征规律，而采用三重孔隙结构模型的预测结果和实验结果能够达到很好的吻合。统计分析了致密油岩石的实验测量结果和模型参数，可推断在5-10% 孔隙度范围内致密油岩石含更多的微裂隙，且在高孔隙度范围微裂隙尺寸更大。在不同孔隙度范围内，微裂隙和黏土包体体积比率相近，但微裂隙尺寸明显大于泥质尺寸，微裂隙体积模量低于泥质体积模量。
关键词：致密油岩石、结构非均质性、岩石物理实验、三重孔隙结构模型、纵波频散和衰减

含黄铁矿泥质砂岩电阻率频散规律实验研究与校正方法//Resistivity dispersion in pyrite-bearing shaly sandstones, 郭志华[1,2]，宋延杰[1,2]，王超[1,3]，唐晓敏[1,2]，**APPLIED GEOPHYSICS**, 16(1), P. 46–55. DOI:10.1007/S11770-019-0745-6

(1、东北石油大学地球科学学院，黑龙江 大庆 163318；2. 非常规油气成藏与开发省部共建国家重点实验室培育基地，黑龙江 大庆 163318；3. 大庆油田有限责任公司第九采油厂地质大队，黑龙江 大庆 163000)

摘要：含黄铁矿泥质岩石的频散特性使得地层的电阻率测井响应值在高频电阻率测井中会出现失真现象，导致储层的饱和度计算存在较大的难度。为了更好的消除岩石中黄铁矿和泥质的电阻率频散影响，同时弥补天然岩心中各种物质成分、含量，以及分布形式等因素无法人工控制的不足，本文设计并在高温高压下制作了12块含分散状黄铁矿颗粒和粘土颗粒的人造固结岩样，分析岩样在多种电流频率条件下，不同地层水矿化度以及饱和度的岩电实验数据，得出频率对含黄铁矿泥质砂岩导电规律的影响：分散状黄铁矿和粘土颗粒都具有频散特性；随着电流频率的增大，岩样复电阻率实部减小。基于有效介质对称导电理论，结合实验研究成果，考虑黄铁矿含量和泥质含量变化对岩石频散规律的影响，建立了黄铁矿泥质砂岩有效介质复电阻率实部频散模型。理论模拟表明当电流频率、黄铁矿及分散泥质含量变化时，模型预测的黄铁矿泥质砂岩频散规律与实验规律相一致。利用岩电实验数据，验证了该模型可以准确地描述含黄铁矿泥质砂岩储层的频散特征。通过选取多种电测井中应用的电流频率，建立了黄铁矿电导率为0.062 S/m，泥质电导率为0.031 S/m的电阻率频率影响校正图版，给出了运用该图版进行高频电阻率测井响应校正的具体方法，为获取地层的真实电阻率值提供了保障。
关键词：黄铁矿，泥质，砂岩，频散，电阻率

一种基于多个GPU的TTI逆时偏移方法//An efficient scheme for multi-GPU TTI reverse time migration, 刘国峰[1*]，孟小红[1]，禹振江[1]，刘定进[2]，**APPLIED GEOPHYSICS**. 2019, **16**(1), P. 56–63. DOI:10.1007/S11770-018-0743-8

(1. 中国地质大学（北京）地球物理与信息技术学院，北京，100083；2. 中国石化石油物探研究院，南京，211103)

摘要：地震数据TTI介质逆时偏移计算量巨大，阻碍了其深度应用。NVIDIA® GPU以及其通用计算具有高度并行特性，为加速该类高密度计算提速提供了可能，可解决由于地震处理成像空间增加所带来的计算量大难题。本文提出了一种高效率的多GPU并行计算策略，以解决TTI介质逆时偏移庞大的数据处理问题。该策略流程，以GPU及其统一设备架构CUDA为前提，拥有多核心同时计算、作业流、点对点GPU直接传输等一些列运算特点。其核心是将GPU间边界数据的数据传输时间和不同区域的差分计算时间重叠。由于逆时偏移计算强度主要与差分计算空间相关。重叠计算后，数据传输时间可以忽略， 因而计算效率随GPU数量的增加呈线性提高。并用于TTI逆时偏移成像的处理， 以验证本文提出的高计算效率的多GPU并行计算策略的正确性。对比试验表明，利用本文提出的多GPU策略可大大提供高密度数据成像计算的效率及实现多GPU计算时效率呈线性增加，提升了该计算的延展特性。